International Journal of Heat and Mass Transfer 75 (2014) 637–649

Contents lists available at ScienceDirect

International Journal of Heat and Mass Transfer

journal homepage: www.elsevier.com/locate/ijhmt

Scaling laws for heat generation and temperature oscillations in EDLCs under galvanostatic cycling

Anna d'Entremont, Laurent Pilon *

University of California, Los Angeles, Henry Samueli School of Engineering and Applied Science, Mechanical and Aerospace Engineering Department, 420 Westwood Plaza, Los Angeles, CA 90095, USA

ARTICLE INFO

Article history:
Received 23 December 2013
Received in revised form 19 March 2014
Accepted 1 April 2014

Keywords:
Supercapacitors
Energy storage
Joule heating
Reversible heating
Dimensional analysis

ABSTRACT

This study provides a framework for developing design rules and thermal management strategies for electric double layer capacitors (EDLCs). First, it presents a scaling analysis of a physical model previously derived from first principles for coupled electrodiffusion and thermal transport in electric double layer capacitors. The model rigorously accounts for irreversible (Joule heating) and reversible heat generation rates arising from electric double layer formation in binary and symmetric electrolytes. Scaling simplified the problem from twelve independent design parameters to seven meaningful dimensionless similarity parameters governing the spatiotemporal evolution of the electric potential, ion concentrations, heat generation rates, and temperature in the electrolyte. Then, similarity behavior was observed and scaling laws were developed for the total irreversible and reversible heat generated during a charging step and for the maximum temperature oscillations in EDLCs under galvanostatic cycling of planar electrodes using detailed numerical simulations.

1. Introduction

Electric double layer capacitors (EDLCs) are devices that store electrical energy within the electric double layer (EDL) forming at the porous electrode/electrolyte interfaces. Their energy and power densities lie between those of batteries and those of conventional dielectric capacitors [1–3]. EDLCs use physical charge storage, in contrast to chemical energy storage used in batteries. This typically yields significantly larger power densities, longer cycle life, and higher cycle efficiencies than batteries [1,3]. In addition, EDLCs use porous electrodes with very small charge separation distances to achieve larger energy densities than dielectric capacitors [1–3]. EDLCs are promising for applications requiring high power, rapid cycling, and long cycle life such as load leveling, regenerative braking, and dynamic stabilization of the utility grid [2,4–7].

During EDLC operation, some electrical energy is dissipated as heat. The device efficiency and the heat generation rate vary with the cell design, materials, and operating conditions [4]. Temperature rise increases EDLC capacitance and decreases the resistance [8–10]. However, it also accelerates EDLC aging [4–7,10,11], and increases self-discharge rates [5–7,10]. EDLC aging permanently increases the cell's resistance and decreases its capacitance, which in turn leads to increases in cell temperature and in cell voltage at a given state of charge [11]. Non-uniform temperature in series-connected EDLC modules can cause voltage imbalance and destructive overvoltage of individual cells [4,7]. A 20% decrease in capacitance or a 100% increase in internal resistance typically define the end of life for an EDLC [12]. These damaging effects could be avoided by mitigating EDLC temperature rise. To do so, thermal modeling can be used (i) to predict operating temperatures of existing and novel EDLC designs and (ii) to develop thermal management strategies for EDLCs.

This study aims to develop a theoretical framework and practical scaling laws to derive rules in the thermal design and management of EDLCs. To do so, scaling analysis was performed on a recent thermal model of EDLCs derived from first principles [13]. The first objective was to reduce the number of design parameters to a few meaningful dimensionless similarity parameters governing the thermal behavior of EDLCs. Then, scaling laws for the heat generation rate and the temperature rise in the electrolyte of EDLCs were developed for planar electrodes.

2. Background

2.1. Structure of the electric double layer

Fig. 1(a) illustrates the Stern model [14,15] of an electric double layer (EDL) forming near a planar electrode. The EDL within the

* Corresponding author. Tel.: +1 (310) 709 2998.
E-mail address: pilon@seas.ucla.edu (L. Pilon).

http://dx.doi.org/10.1016/j.ijheatmasstransfer.2014.04.001
0017-9310/

Nomenclature

A	semi-empirical fitting function
a	effective ion diameter
B	semi-empirical fitting function
C^*	dimensionless heat capacity
c	ion concentration
c_{max}	maximum ion concentration, $c_{max} = 1/N_A a^3$
c_p	specific heat of the electrolyte at constant pressure
D	diffusion coefficient of ions in electrolyte
e	elementary charge, $e = 1.602 \times 10^{-19}$ C
e_{th}	thermal effusivity, $e_{th} = (k\rho c_p)^{1/2}$
F	Faraday constant, $F = eN_A = 9.648 \times 10^4$ C mol^{-1}
H	Stern layer thickness
$\mathbf{j}$	ionic current density vector
j_s	magnitude of current density imposed at electrode surface
k	thermal conductivity of electrolyte
L	half of inter-electrode distance
Le	Lewis number, $Le = \alpha/D$
N_A	Avogadro constant, $N_A = 6.022 \times 10^{23}$ mol^{-1}
$\mathbf{N}_i$	ion flux vector of species i
n_c	cycle number
Q	amount of heat generated per charging step per unit surface area
$\dot{q}$	local volumetric heat generation rate
R_u	universal gas constant, $R_u = 8.314$ J mol^{-1} K^{-1}
$\mathbf{r}$	location vector in three-dimensional space
T	local, absolute temperature
T_0	initial temperature
t	time
t_c	cycle period
x	location in one-dimensional space
z	ion valency

Greek symbols

α	thermal diffusivity, $\alpha = k/\rho c_p$
ϵ_0	vacuum permittivity, $\epsilon_0 = 8.854 \times 10^{-12}$ F m^{-1}
ϵ_r	relative permittivity of electrolyte
λ_D	Debye length
ν_p	packing parameter, $\nu_p = 2c_\infty N_A a^3$
ρ	density of electrolyte
σ	electrical conductivity of electrolyte
τ_d	characteristic time for ion diffusion across EDL
τ_{th}	characteristic time for heat diffusion across EDL
ψ	electric potential

Superscripts and subscripts

$*$	refers to dimensionless variable
∞	refers to bulk electrolyte
E, d	refers to heat generation due to diffusion
E, s	refers to heat generation due to steric effects
i	refers to ion species i
irr	refers to irreversible heat generation
rev	refers to reversible heat generation
S, c	refers to heat of mixing due to concentration gradient
S, T	refers to heat of mixing due to temperature gradient

electrolyte is divided into the Stern and diffuse layers. The Stern layer is defined as the compact layer adjacent to the electrode surface with no free charge [3,14,15]. In the diffuse layer, ions move under the coupled influences of electrostatic forces and diffusion [3,14,15]. The EDL thickness depends on the electrolyte concentration, valency, and temperature [14,15].

2.2. First-principles modeling of EDLC transport phenomena

In a recent study [13], we developed a thermal model predicting the local heat generation rate and temperature within EDLC electrolyte. The energy conservation equation was derived from first principles and coupled to the modified Poisson–Nernst–Planck (MPNP) model governing the local electric potential and ion concentrations [16]. Both were valid for binary and symmetric electrolytes, i.e., for only two ion species with identical valency z, diffusion coefficient D, and effective diameter a [16]. Note that symmetric electrolytes have also been defined based on symmetric valency alone, i.e., $z_1 = -z_2$, without considering the ion diameter or the diffusion coefficient [1,14,15]. However, microscopic models accounting for transient ion transport and finite ion size require a more restrictive definition of electrolyte symmetry. The thermal model was derived based on the thermodynamic activity coefficients of the ion species given by the Debye–Hückel limiting law [17,18].

2.2.1. Electric potential and ion concentrations

The local electric potential and ion concentrations in the electrolyte can be predicted by solving the modified Poisson–Nernst–Planck (MPNP) model accounting for the Stern layer and the finite size of ions [13,16]. The electric potential $\psi(\mathbf{r}, t)$ at location $\mathbf{r}$ and time t is governed by the Poisson equation expressed for binary electrolytes as [13,16,19,20]

$$\nabla \cdot (\epsilon_0 \epsilon_r \nabla \psi) = \begin{cases} 0 & \text{in the Stern layers,} \\ -F \sum_{i=1}^{2} z_i c_i & \text{in the diffuse layer,} \end{cases} \tag{1}$$

where $c_i(\mathbf{r}, t)$ and z_i denote the concentration and valency of ion species i, respectively. For binary and symmetric electrolytes, $z_1 = -z_2 = z$ where subscripts $i = 1$ and $i = 2$ denote cations and anions, respectively. Here, $\epsilon_0 = 8.854 \times 10^{-12}$ F mol^{-1} and ϵ_r are the vacuum permittivity and the relative permittivity of the electrolyte, respectively, while $F = 9.648 \times 10^4$ C mol^{-1} is the Faraday constant. Note that the potential profile within the Stern layers is linear due to the absence of free charge. In the diffuse layer, the local concentrations $c_1(\mathbf{r}, t)$ and $c_2(\mathbf{r}, t)$ satisfy the mass conservation equation given by [16]

$$\frac{\partial c_i}{\partial t} = -\nabla \cdot \mathbf{N}_i \quad \text{for } i = 1 \text{ and } 2, \tag{2}$$

where $\mathbf{N}_i(\mathbf{r}, t)$ is the local ion flux vector of species i in mol m^{-2} s^{-1}. For binary and symmetric electrolytes, it is expressed as [16]

$$\mathbf{N}_i(\mathbf{r}, t) = -\left[D\nabla c_i + \frac{z_i F D}{R_u T} c_i \nabla \psi + \frac{D a^3 N_A c_i}{1 - a^3 N_A (c_1 + c_2)} \nabla (c_1 + c_2) \right], \tag{3}$$

where the first, second, and third terms on the right-hand side of Eq. (3) account for diffusion, electromigration, and steric effects, respectively. The steric term prevents the total ion concentration $(c_1 + c_2)$ from exceeding the theoretical maximum concentration $c_{max} = 1/N_A a^3$ corresponding to simple cubic packing of ions. Here, D is the diffusion coefficient of ions in the electrolyte, a is their effective diameter, $R_u = 8.314$ J mol^{-1} K^{-1} is the universal gas constant, and $N_A = 6.022 \times 10^{23}$ mol^{-1} is the Avogadro constant. Eqs. (1) and (2) are intimately coupled because the potential profile

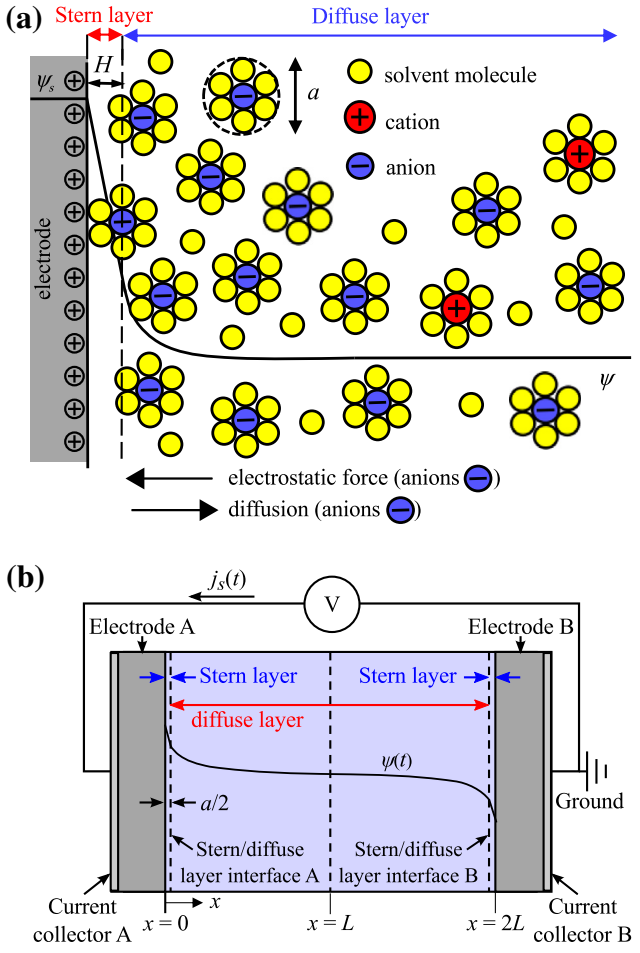

Fig. 1. Illustration of (a) electric double layer structure near a planar electrode, according to the Stern model [14,15] and (b) the simulated EDLC planar electrodes.

depends on the ion concentration distribution and vice versa. The effect of temperature on the electric potential and ion concentrations is accounted for by the temperature-dependent electrolyte properties such as the diffusion coefficient D and by the presence of the local temperature T in the electromigration term.

2.2.2. Heat generation rate and temperature

The temperature $T(\mathbf{r},t)$ in the electrolyte is governed by the energy conservation equation expressed as [13,21]

$$\rho c_p \frac{\partial T}{\partial t} = \nabla \cdot (k \nabla T) + \dot{q}, \tag{4}$$

where ρ, c_p, and k are respectively the density, specific heat, and thermal conductivity of the electrolyte. The local volumetric heat generation rate $\dot{q}(\mathbf{r},t)$ can be divided into an irreversible $\dot{q}_{irr}$ and a reversible $\dot{q}_{rev}$ contribution so that $\dot{q} = \dot{q}_{irr} + \dot{q}_{rev}$.

The irreversible volumetric heat generation rate corresponds to Joule heating within the electrolyte and is expressed as [13]

$$\dot{q}_{irr}(\mathbf{r},t) = \frac{|\mathbf{j}|^2}{\sigma}, \tag{5}$$

where the local ionic current density vector $\mathbf{j}$ and the electrolyte's electrical (ionic) conductivity σ are respectively defined as [17,22]

$$\mathbf{j}(\mathbf{r},t) = \sum_{i=1}^{2} z_i F \mathbf{N}_i(\mathbf{r},t) \quad \text{and}$$
$$\sigma(\mathbf{r},t) = (Dz^2F^2/R_uT)[c_1(\mathbf{r},t) + c_2(\mathbf{r},t)]. \tag{6}$$

Irreversible heat generation is responsible for the overall temperature rise from cycle to cycle observed experimentally during galvanostatic cycling [4–6,10,23–25]. Eq. (5) is consistent with the experimental observation that the irreversible heating was proportional to the imposed electric current squared [6].

The reversible volumetric heat generation rate $\dot{q}_{rev}(\mathbf{r},t)$ comprises four contributions and is expressed as [13]

$$\dot{q}_{rev} = \dot{q}_{E,d} + \dot{q}_{E,s} + \dot{q}_{S,c} + \dot{q}_{S,T}, \tag{7}$$

where $\dot{q}_{E,d}$ and $\dot{q}_{E,s}$ denote the heat generation rates due to ion diffusion and steric effects within an electric field, respectively. They are expressed for binary and symmetric electrolytes as [13]

$$\dot{q}_{E,d}(\mathbf{r},t) = \frac{DzF}{\sigma}\mathbf{j} \cdot \nabla(c_1 - c_2) \quad \text{and}$$
$$\dot{q}_{E,s}(\mathbf{r},t) = \frac{DzFa^3N_A(c_1 - c_2)}{\sigma[1 - a^3N_A(c_1 + c_2)]}\mathbf{j} \cdot \nabla(c_1 + c_2). \tag{8}$$

In addition, $\dot{q}_{S,c}$ and $\dot{q}_{S,T}$ correspond to the heat of mixing associated with ion flow along the partial molar entropy gradient and along the temperature gradient. They are given by [13]

$$\dot{q}_{S,c}(\mathbf{r},t) = \frac{3}{32\pi}\frac{z^3eF^2}{(\epsilon_0\epsilon_r)^{3/2}R_u^{1/2}T^{1/2}(c_1 + c_2)^{1/2}}(\mathbf{N}_1 + \mathbf{N}_2) \cdot \nabla(c_1 + c_2)$$
$$\text{and} \quad \dot{q}_{S,T}(\mathbf{r},t) = -\frac{3}{32\pi}\frac{z^3eF^2(c_1 + c_2)^{1/2}}{(\epsilon_0\epsilon_r)^{3/2}R_u^{1/2}T^{3/2}}(\mathbf{N}_1 + \mathbf{N}_2) \cdot \nabla T \tag{9}$$

where e is the elementary charge $e = 1.602 \times 10^{-19}$ C. The reversible heat generation rates $\dot{q}_{E,d}$, $\dot{q}_{E,s}$, and $\dot{q}_{S,c}$ are exothermic during charging and endothermic during discharging [6,13,24], while $\dot{q}_{S,T}$ was found to be negligible compared to the other contributions for the conditions tested in Ref. [13]. The above expressions are consistent with observations from galvanostatic cycling experiments indicating that the reversible heat generation rate was proportional to the current density [24,25]. This model was used to numerically simulate the electrolyte temperature near planar electrodes under galvanostatic cycling [13]. The temperature predictions showed excellent qualitative agreement with experimental temperature measurements from the literature for commercial EDLC devices with porous carbon electrodes tested under different galvanostatic cycling conditions [13].

Scaling analysis has proved to be a useful and powerful tool in numerous areas of physics and engineering, particularly in heat transfer [21]. Scaling of the above governing Eqs. (1)–(9) and of the associated initial and boundary conditions could significantly reduce the number of independent parameters that must be considered in performing thermal analysis of EDLC electrolytes. This can facilitate the development of thermal design rules to mitigate EDLC heating applicable to a wide range of electrolytes and operating conditions.

3. Analysis

3.1. Problem statement

Fig. 1(b) illustrates the simulated one-dimensional EDLC consisting of two planar electrodes separated by a binary and symmetric electrolyte with inter-electrode distance $2L$. The planar electrodes located at $x = 0$ and $x = 2L$ were denoted as electrodes A and B, respectively. The electrolyte was divided into three regions: a Stern layer adjacent to each electrode and a diffuse layer. We further assume that (1) the electrolyte properties were constant and independent of temperature, except for the electrical conductivity calculated from the local ion concentrations (Eq. (6)). (2) The Stern layer thickness H was equal to half of the effective ion diameter, i.e., $H = a/2$, and (3) the EDLC was thermally

insulated. The present study models only the electrolyte. In EDLC devices, electrodes and current collectors also contribute to irreversible Joule heating and to the thermal inertia. Electrodes and current collectors obey Ohm's law [17] and do not contribute to the reversible heating. Note also that the electrical conductivity of the electrode and current collector materials are expected to be much larger than that of the electrolyte. For example, the bulk electrical conductivity σ_∞ of the electrolyte considered in Ref. [13] and the present study was on the order of 1 S m^{-1} while the conductivity of activated carbon is on the order of 100–1000 S m^{-1} [26–28]. Thus, the electrolyte is the dominant source of heat generation in the device. Assumption (1) is reasonable for small changes in temperature and commonly used for scaling analysis. Thus, the temperature T appearing in the expressions for $\mathbf{N}_i$, $\dot{q}_{S,c}$, and $\dot{q}_{S,T}$ was taken as the initial temperature T_0. Note that the thermal behavior of EDLCs is intrinsically transient, as ion fluxes responsible for the heat generation vanish at equilibrium.

3.2. Initial and boundary conditions for planar electrodes

In one-dimensional (1D) Cartesian coordinates, the governing Eqs. (1)–(4) for $\psi(x,t)$, $c_i(x,t)$, and $T(x,t)$ are first-order partial differential equations (PDEs) in time and second-order PDEs in space. They require one initial condition and two boundary conditions in each region. The present study considers the electrolyte region $0 \leqslant x \leqslant 2L$ only. Eqs. (1) and (4) were solved in all three layers of the electrolyte while Eq. (2) was solved in the diffuse layer only. Initially, the potential, ion concentrations, and temperature were taken as uniform throughout the electrolyte domain $0 \leqslant x \leqslant 2L$ and equal to $\psi(x,0) = 0$ V, $c_1(x,0) = c_2(x,0) = c_\infty$, and $T(x,0) = T_0$, respectively. Table 1 summarizes the boundary conditions at the electrode/electrolyte and Stern/diffuse layer interfaces during galvanostatic charging and discharging of a thermally insulated EDLC under current density $\pm j_s$ with cycle period t_c. Here, $n_c = 1, 2, 3\ldots$ is the cycle number. These initial and boundary conditions are the same as those used in Ref. [13].

3.3. Scaling analysis

3.3.1. Dimensionless variables

Eqs. (1)–(9) along with the associated initial and boundary conditions were non-dimensionalized using the dimensionless variables

$$\mathbf{r}^* = \frac{\mathbf{r}}{\lambda_D}, \quad t^* = \frac{t}{\lambda_D^2/D}, \quad \psi^*(x^*,t^*) = \frac{\psi(x,t)}{R_u T_0/zF},$$
$$c_i^*(x^*,t^*) = \frac{c_i(x,t)}{c_\infty}, \quad \text{and} \quad T^*(x^*,t^*) = \frac{T(x,t)-T_0}{T_0}. \tag{10}$$

Here, the position vector $\mathbf{r}$ was scaled by the Debye length defined for binary and symmetric electrolyte as $\lambda_D = \sqrt{\epsilon_0\epsilon_r R_u T_0/2z^2F^2c_\infty}$ and corresponding to an estimate of the EDL thickness at temperature T_0 [22,29,30]. Specifically, it characterizes the distance required for the potential to decay by about 66% from its value at the electrode surface [30]. The time t was scaled by the characteristic time for ion diffusion across the EDL thickness estimated as $\tau_d = \lambda_D^2/D$ [21]. The thermal voltage R_uT_0/zF represents the voltage inducing an electrical potential energy equivalent to the thermal energy for an ion of valency z at temperature T_0 [22]. Thus, the dimensionless surface potential ψ^* characterizes the extent to which the potential ψ perturbs the ion concentrations from their equilibrium distribution under zero electric field. Finally, the concentration $c_i(x,t)$ and the temperature change $T(x,t) - T_0$ were scaled by the bulk ion concentration c_∞ and the initial temperature T_0, respectively.

Using the scaled position vector $\mathbf{r}^*$, the gradient, divergence, and Laplacian operators can be respectively non-dimensionalized as

$$\nabla^* f^*(\mathbf{r}^*) = \frac{\lambda_D}{f_0}\nabla f, \quad \nabla^* \cdot \mathbf{v}^*(\mathbf{r}^*) = \frac{\lambda_D}{v_0}\nabla\cdot\mathbf{v}, \quad \text{and} \quad \nabla^{*2} f^* = \frac{\lambda_D^2}{f_0}\nabla^2 f, \tag{11}$$

where the function $f(\mathbf{r})$ and the vector $\mathbf{v}$ are scaled by the scalars f_0 and v_0, respectively so that $f^* = f/f_0$ and $\mathbf{v}^* = \mathbf{v}/v_0$.

3.3.2. Dimensionless Poisson equation

Substituting Eq. (10) into the 1D Poisson equation (1) yields the following governing equation for the dimensionless electric potential $\psi^*(x^*,t^*)$ [31]

$$-2\nabla^{*2}\psi^* = \begin{cases} 0 & \text{in the Stern layers,} \\ c_1^* - c_2^* & \text{in the diffuse layer.} \end{cases} \tag{12}$$

3.3.3. Dimensionless mass conservation equation

The dimensionless concentrations $c_i^*(x^*,t^*)$ of the cations and anions in the diffuse layer satisfy the dimensionless 1D mass conservation equations expressed as

$$\frac{\partial c_i^*}{\partial t^*} = -\nabla^*\cdot\mathbf{N}_i^* \quad i = 1 \text{ and } 2. \tag{13}$$

Table 1
Dimensional and dimensionless boundary conditions for thermally insulated EDLC with planar electrodes during galvanostatic cycling.

Interface	ψ	c_i	T
Electrode A/electrolyte ($x = 0$ nm)	$-\epsilon_0\epsilon_r\frac{\partial^2\psi}{\partial t\partial x} = \begin{cases} j_s & (n_c-1)t_c \leqslant t < (n_c-1/2)t_c \\ -j_s & (n_c-1/2)t_c \leqslant t < n_c t_c \end{cases}$		$-k\frac{\partial T}{\partial x} = 0\,\frac{\text{W}}{\text{m}^2}$
Stern/diffuse layer A ($x = H = a/2$)	$\psi(H^-,t) = \psi(H^+,t)$	$N_i = 0\,\frac{\text{mol}}{\text{m}^2\,\text{s}}$	$T(H^-,t) = T(H^+,t)$
	$\frac{\partial\psi}{\partial x}(H^-,t) = \frac{\partial\psi}{\partial x}(H^+,t)$		$\frac{\partial T}{\partial x}(H^-,t) = \frac{\partial T}{\partial x}(H^+,t)$
Stern/diffuse layer B ($x = 2L - H$)	$\psi(2L-H^-,t) = \psi(2L-H^+,t)$	$N_i = 0\,\frac{\text{mol}}{\text{m}^2\,\text{s}}$	$T(2L-H^-,t) = T(2L-H^+,t)$
	$\frac{\partial\psi}{\partial x}(2L-H^-,t) = \frac{\partial\psi}{\partial x}(2L-H^+,t)$		$\frac{\partial T}{\partial x}(2L-H^-,t) = \frac{\partial T}{\partial x}(2L-H^+,t)$
Electrode B/electrolyte ($x = 2L$)	$\psi = 0$V		$-k\frac{\partial T}{\partial x} = 0\,\frac{\text{W}}{\text{m}^2}$
	ψ^*	c_i^*	T^*
Electrode A/electrolyte ($x^* = 0$)	$-\frac{\partial^2\psi^*}{\partial t^*\partial x^*} = \begin{cases} \frac{j_s^*}{2} & (n_c-1)t_c^* \leqslant t^* < (n_c-1/2)t_c^* \\ -\frac{j_s^*}{2} & (n_c-1/2)t_c^* \leqslant t^* < n_c t_c^* \end{cases}$		$\frac{\partial T^*}{\partial x^*} = 0$
Stern/diffuse layer A ($x^* = a^*/2$)	$\psi^*(\frac{a^-}{2},t^*) = \psi^*(\frac{a^+}{2},t^*)$	$N_i^* = 0$	$T^*(\frac{a^-}{2},t^*) = T^*(\frac{a^+}{2},t^*)$
	$\frac{\partial\psi^*}{\partial x^*}(\frac{a^-}{2},t^*) = \frac{\partial\psi^*}{\partial x^*}(\frac{a^+}{2},t^*)$		$\frac{\partial T^*}{\partial x^*}(\frac{a^-}{2},t^*) = \frac{\partial T^*}{\partial x^*}(\frac{a^+}{2},t^*)$
Stern/diffuse layer B ($x^* = 2L^* - a^*/2$)	$\psi^*(2L^*-\frac{a^-}{2},t^*) = \psi^*(2L^*-\frac{a^+}{2},t^*)$	$N_i^* = 0$	$T^*(2L^*-\frac{a^-}{2},t^*) = T^*(2L^*-\frac{a^+}{2},t^*)$
	$\frac{\partial\psi^*}{\partial x^*}(2L^*-\frac{a^-}{2},t^*) = \frac{\partial\psi^*}{\partial x^*}(2L^*-\frac{a^+}{2},t^*)$		$\frac{\partial T^*}{\partial x^*}(2L^*-\frac{a^-}{2},t^*) = \frac{\partial T^*}{\partial x^*}(2L^*-\frac{a^+}{2},t^*)$
Electrode B/electrolyte ($x^* = 2L^*$)	$\psi^* = 0$		$\frac{\partial T^*}{\partial x^*} = 0$

The dimensionless local ion flux vector $\mathbf{N}_i^*(x^*,t^*)$ is defined as $\mathbf{N}_i^* = \mathbf{N}_i/(Dc_\infty/\lambda_D)$ and expressed for binary and symmetric electrolytes as

$$\mathbf{N}_i^* = -\left[\nabla^* c_i^* + \mathrm{sgn}(z_i) c_i^* \nabla^* \psi^* + \frac{c_i^* v_p/2}{1-(c_1^*+c_2^*)v_p/2}\nabla^*(c_1^*+c_2^*)\right]. \tag{14}$$

Here, the dimensionless number $v_p = 2c_\infty/c_{max} = 2c_\infty N_A a^3$ is the so-called packing parameter corresponding to the ratio of the total bulk concentration $2c_\infty$ to the theoretical maximum concentration c_{max} [16]. It is less than unity as the bulk concentration cannot exceed c_{max}. It approaches zero in the limiting case of negligibly small ion diameter a. The function $\mathrm{sgn}(z_i)$ is equal to +1 or −1 depending on the sign of the valency z_i.

3.3.4. Dimensionless energy conservation equation

The dimensionless energy equation derived from Eq. (4) can be expressed as

$$\frac{\partial T^*}{\partial t^*} = Le\nabla^{*2}T^* + \frac{\dot{q}^*}{C^*}. \tag{15}$$

The Lewis number Le is defined as $Le = \alpha/D$ where $\alpha = k/\rho c_p$ is the thermal diffusivity [21]. The dimensionless heat capacity C^* is defined as $C^* = \rho c_p/R_u c_\infty$. Here, the dimensionless local volumetric heat generation rate is given by $\dot{q}^* = \dot{q}/(R_u T_0 D c_\infty/\lambda_D^2) = \dot{q}_{irr}^* + \dot{q}_{rev}^*$ where $\dot{q}_{rev}^* = \dot{q}_{E,d}^* + \dot{q}_{E,s}^* + \dot{q}_{S,c}^* + \dot{q}_{S,T}^*$. The irreversible Joule heating $\dot{q}_{irr}$ is expressed in dimensionless form as

$$\dot{q}_{irr}^* = \frac{|\mathbf{j}^*|^2}{c_1^*+c_2^*}, \tag{16}$$

where $\mathbf{j}^* = \mathbf{j}/(zFDc_\infty/\lambda_D) = \mathbf{N}_1^* - \mathbf{N}_2^*$ is the dimensionless local current density vector. The diffusion and steric contributions $\dot{q}_{E,d}$ and $\dot{q}_{E,s}$ are expressed in dimensionless form as

$$\dot{q}_{E,d}^* = \frac{\mathbf{j}^*\cdot\nabla^*(c_1^*-c_2^*)}{c_1^*+c_2^*} \quad \text{and}$$
$$\dot{q}_{E,s}^* = \frac{\mathbf{j}^*\cdot\nabla^*(c_1^*+c_2^*)}{c_1^*+c_2^*}\frac{(c_1^*-c_2^*)v_p/2}{[1-(c_1^*+c_2^*)v_p/2]}, \tag{17}$$

while the heat of mixing contributions $\dot{q}_{S,c}$ and $\dot{q}_{S,T}$ can be non-dimensionalized as

$$\dot{q}_{S,c}^* = \frac{3}{32\sqrt{2}\pi}\frac{a^{*3}}{v_p}\frac{(\mathbf{N}_1^*+\mathbf{N}_2^*)\cdot\nabla^*(c_1^*+c_2^*)}{(c_1^*+c_2^*)^{1/2}},$$
$$\text{and} \quad \dot{q}_{S,T}^* = -\frac{3}{32\sqrt{2}\pi}\frac{a^{*3}}{v_p}(\mathbf{N}_1^*+\mathbf{N}_2^*)(c_1^*+c_2^*)^{1/2}\cdot\nabla^* T^*. \tag{18}$$

Here, $a^* = a/\lambda_D$ is the dimensionless effective ion diameter.

3.4. Dimensionless initial and boundary conditions for planar electrodes

In 1D Cartesian coordinates, the initial conditions for the dimensionless variables ψ^*, c_i^*, and T^* can be expressed as $\psi^*(x^*,0) = 0$, $c_1^*(x^*,0) = c_2^*(x^*,0) = 1$, and $T^*(x^*,0) = 0$. Table 1 summarizes the dimensionless boundary conditions for ψ^*, c_i^*, and T^* at the electrode/electrolyte and Stern/diffuse layer interfaces. The Stern layers for electrodes A and B are located at $0 \le x^* < a^*/2$ and $(2L^* - a^*/2) < x^* \le 2L^*$, respectively. The diffuse layer is the region $a^*/2 \le x^* \le 2L^* - a^*/2$ where $L^* = L/\lambda_D$ is the dimensionless inter-electrode half-width. Here, $j_s^* = j_s/(zFDc_\infty/\lambda_D)$ is the dimensionless current density imposed at the electrode surface and $t_c^* = t_c/(\lambda_D^2/D)$ is the dimensionless cycle period.

3.5. Physical interpretation

The solution of the governing Eqs. (1)–(4) and their initial and boundary conditions for galvanostatic cycling of planar EDLCs with binary and symmetric electrolyte depended on twelve parameters, namely z, a, D, ϵ_r, ρ, c_p, k, c_∞, L, T_0, j_s, and t_c. The scaling analysis of these equations and their initial and boundary conditions revealed that the dimensionless variables ψ^*, c_i^*, and T^* depended on only seven dimensionless similarity parameters expressed as

$$a^* = \frac{a}{\lambda_D}, \quad L^* = \frac{L}{\lambda_D}, \quad j_s^* = \frac{j_s}{zFDc_\infty/\lambda_D},$$
$$t_c^* = \frac{t_c}{\lambda_D^2/D} \quad v_p = \frac{2c_\infty}{c_{max}}, \quad Le = \frac{\alpha}{D}, \quad \text{and} \quad C^* = \frac{\rho c_p}{R_u c_\infty}. \tag{19}$$

The dimensionless numbers a^* and L^* scale the Stern layer thickness and the inter-electrode distance by the Debye length, respectively. The dimensionless current density j_s^* scales the imposed current density at the electrode by a characteristic diffusion current density driven by a concentration gradient from c_∞ to 0 mol/L across the Debye length λ_D (equal to the concentration drop of the co-ion across the EDL). In addition, t_c^* is the ratio of the cycle period to the characteristic time $\tau_d = \lambda_D^2/D$ for ion diffusion across the Debye length. The Lewis number Le can be interpreted as the ratio of the characteristic time for ion diffusion $\tau_d = \lambda_D^2/D$ to that for heat diffusion $\tau_{th} = \lambda_D^2/\alpha$. The dimensionless heat capacity C^* represents the ratio of the volumetric heat capacity ρc_p of the solvent to that of the ions at bulk concentration $R_u c_\infty$, both expressed in J m^{-3} K^{-1}.

Finally, $\psi^*(x^*,t^*)$ and $c_i^*(x^*,t^*)$ are functions of the dimensionless similarity parameters a^*, L^*, j_s^*, t_c^*, and v_p only. On the other hand, the Lewis number Le and the dimensionless heat capacity C^* govern the transient dimensionless temperature response $T^*(x^*,t^*)$ for a given dimensionless volumetric heat generation rate. Since the dimensionless volumetric heat generation rates $\dot{q}_{irr}^*$, $\dot{q}_{E,d}^*$, $\dot{q}_{E,s}^*$, and $\dot{q}_{S,c}^*$ do not depend on T^*, Le, or C^*, they should also be functions of the five parameters a^*, L^*, j_s^*, t_c^*, and v_p.

3.6. Numerical simulations

3.6.1. Method of solution

The governing Eqs. (1)–(4) were solved for a planar EDLC in dimensional form using finite element methods. Numerical convergence was assessed based on the computed local electric potential ψ, ion concentrations c_1 and c_2, and temperature T at time t. Of these quantities, the temperature was the most sensitive to mesh refinement. The mesh size was the smallest at the Stern/diffuse layer interface due to the large potential and concentration gradients and then gradually increased away from this interface. The mesh was refined by reducing the element size at the Stern/diffuse layer interface and the maximum element growth rate. The time step was refined by decreasing the relative and absolute tolerances [32]. During each time step, these tolerances were compared to the estimated local error between solutions at the previous and current time steps for each degree of freedom in the model [32]. The time step was then adjusted until the convergence criterion was satisfied, as described in Ref. [32]. This enabled the use of very small time steps near the transitions between charging and discharging steps while using a larger time step for the rest of the computation. The numerical solution was considered converged when halving (i) the element size at the Stern/diffuse layer interface, (ii) the maximum element growth rate, and (iii) both the relative and absolute tolerances resulted in less than 0.5% maximum relative difference in the local temperature rise $T(x,t) - T_0$.

3.6.2. Data processing

The temperature evolution is characterized by the irreversible temperature rise T_{irr}, the temperature oscillation amplitude ΔT_{rev}, and the cycle period t_c [13]. The irreversible temperature rise T_{irr} corresponds to the temperature that would result from irreversible Joule heating alone. Our previous study [13] showed that $\dot{q}_{irr}$ was uniform through the electrolyte and equal to

$$\dot{q}_{irr} = \frac{j_s^2}{\sigma_\infty}, \tag{20}$$

where $\sigma_\infty = 2Dz^2F^2c_\infty/R_uT_0$ is the electrolyte conductivity at the bulk concentration $c_1 = c_2 = c_\infty$. Thus, assuming insulated electrode/electrolyte interfaces, T_{irr} was also uniform and expressed as

$$T_{irr}(t) = T_0 + \frac{\dot{q}_{irr}}{\rho c_p}t = T_0 + \frac{j_s^2}{\rho c_p \sigma_\infty}t. \tag{21}$$

The irreversible volumetric heat generation rate and the irreversible temperature rise given by Eqs. (20) and (21), respectively, are expressed in dimensionless form as

$$\dot{q}^*_{irr} = \frac{\dot{q}_{irr}}{R_uT_0Dc_\infty/\lambda_D^2} = \frac{j_s^{*2}}{2} \quad \text{and} \quad T^*_{irr}(t^*) = \frac{T_{irr}(t)-T_0}{T_0} = \frac{\dot{q}^*_{irr}}{C^*}t^* = \frac{j_s^{*2}}{2C^*}t^*. \tag{22}$$

The temperature oscillations $T_{rev}(x,t)$ associated with the reversible heating can be evaluated by subtracting the irreversible temperature rise $T_{irr}(t)$ from the temperature $T(x,t)$, i.e., $T_{rev}(x,t) = T(x,t) - T_{irr}(t)$. The temperature oscillations varied with location x due to the non-uniformity of $\dot{q}_{rev}$ [13]. For temperature-independent electrolyte properties and ion transport, $T_{rev}(x,t)$ was a periodic function of t. In the present study, the oscillation amplitude $\Delta T_{rev}(x)$ was evaluated at the Stern/diffuse layer interface where it was found to be the largest [13]. It was defined as $\Delta T_{rev}(a/2) = \max_{t_c\leqslant t\leqslant 2t_c}[T_{rev}(a/2,t)] - \min_{t_c\leqslant t\leqslant 2t_c}[T_{rev}(a/2,t)]$ and was an unknown function of the twelve parameters characterizing the electrolyte, inter-electrode spacing, and cycling conditions. In dimensionless form, the reversible temperature evolution and the oscillation amplitude are expressed as $T^*_{rev}(x^*,t^*) = T_{rev}(x,t)/T_0 = T^*(x^*,t^*) - T^*_{irr}(t^*)$ and $\Delta T^*_{rev}(a^*/2) = \Delta T_{rev}(a/2)/T_0$. Based on the above dimensional analysis, one can show that ΔT^*_{rev} is a function of the seven similarity parameters identified in Eq. (19). The parameters j_s^* and ν_p do not affect ΔT^*_{rev} directly, but they affect the value of $\dot{q}^*_{rev}$. A correlation relating ΔT^*_{rev} to these seven parameters would enable predictions of the EDLC temperature evolution for various design and operating parameters without performing complex and time-consuming numerical simulations [13].

Finally, the reversible heat generation rate was characterized by the total amount of reversible heat Q_{rev} generated per unit electrode surface area during a complete charging step (in J m^{-2}). Here, Q_{rev} comprises the sum of all reversible contributions such that $Q_{rev} = Q_{E,d} + Q_{E,s} + Q_{S,c}$. Individual Q_i were computed by integrating the corresponding local volumetric heat generation rate $\dot{q}_i(x,t)$ spatially over the electrolyte domain $0 \leqslant x \leqslant 2L$ and temporally over one charging step $t_c \leqslant t \leqslant 3t_c/2$ so that

$$Q_i = \int_{t_c}^{3t_c/2}\int_0^{2L} \dot{q}_i(x,t)dxdt. \tag{23}$$

Here, the time integral was taken over the second charging step in the simulation, i.e., $t_c \leqslant t \leqslant 3t_c/2$, to avoid start-up effects occurring near $t = 0$. Longer simulations showed that two cycles were sufficient to reach oscillatory steady state. In dimensionless form, each individual contribution to the reversible heat generation is expressed as

$$Q_i^* = \frac{Q_i}{R_uT_0c_\infty\lambda_D} = \int_{t_c^*}^{3t_c^*/2}\int_0^{2L^*} \dot{q}_i^*(x^*,t^*)dx^*dt^*. \tag{24}$$

Note that $Q_{S,T}$ was ignored because its contribution to the total Q_{rev} was negligible for all cases considered. During the corresponding discharging step ($3t_c/2 \leq t \leq 2t_c$), the energy $-Q_i$ was consumed so that the net reversible heat generation over a complete charging/discharging cycle was zero.

4. Results and discussion

4.1. Illustration of scaling analysis

Table 2 summarizes three sets of input parameters used to illustrate the scaling analysis. Case 1 was based on the properties of tetraethylammonium tetrafluoroborate ($TEABF_4$) electrolyte at 1 mol L^{-1} in propylene carbonate (PC) solvent. This electrolyte was treated as binary and symmetric. The ions TEA^+ ($i = 1$) and BF_4^- ($i = 2$) have valency $z_1 = -z_2 = 1$. Their effective diameter was taken as that of non-solvated TEA^+ ions, i.e., $a = 0.68$ nm [33,34]. In fact, Wang and Pilon [34] found that using this ion diameter resulted in predictions of the integral capacitance of ordered bimodal mesoporous carbon electrodes in good agreement with experimental data. The dielectric constant ϵ_r, thermal conductivity k, density ρ, and specific heat c_p were taken as the properties of the PC solvent [35,36]. The ion diffusion coefficient D was estimated from the experimentally measured electrical conductivity σ for a concentration of $c_1 = c_2 = c_\infty = 1$ mol/L using the expression given in Eq. (6) [37]. The electrolyte properties ϵ_r, k, ρ, c_p, and σ were measured at temperatures within 5 K of the simulated initial temperature $T_0 = 298$ K [37,35,36]. The inter-electrode half-width $L = 20$ μm fell within the range reported in experimental studies of EDLCs [23,24]. Similarly, the current density $j_s = 14$ mA cm^{-2} was within the typical range of current densities per unit separator surface area [6,24]. The cycle period $t_c = 10$ ms was selected to yield a maximum voltage of $\psi(0,t) - \psi(2L,t) = 2.5$ V chosen by analogy with the operating voltages of many commercial EDLCs using organic electrolytes [1,38]. Note that planar electrodes charge very rapidly compared to porous electrodes, resulting in a significantly shorter cycle period.

The dimensionless numbers associated with Case 1 were $a^* = 2.4$, $L^* = 7.2\times10^4$, $j_s^* = 2.4\times10^{-6}$, $t_c^* = 2.2\times10^7$, $\nu_p = 0.38$, $Le = 374$, and $C^* = 310$. The dimensionless governing Eqs. (12), (13), and (15) and their associated initial and boundary conditions indicate that the dimensionless solution for ψ^*, c_1^*, c_2^*, and T^* depends only on the seven dimensionless numbers defined in Eq. (19). To illustrate this, the twelve input parameters z, a, D, ϵ_r, ρ, c_p, k, c_∞, L, T_0, j_s, and t_c for Cases 2 and 3 were all varied arbitrarily, while the seven

Table 2
Input parameters for Cases 1 to 3 used to illustrate the scaling analysis. The dimensionless parameters $a^* = 2.4$, $L^* = 7.2\times10^4$, $j_s^* = 2.4\times10^{-6}$, $t_c^* = 2.2\times10^7$, $\nu_p = 0.38$, $Le = 374$, and $C^* = 310$ are the same for all three cases.

	Case 1	Case 2	Case 3
z	1	1	2
a (nm)	0.68	0.34	1.36
D (m^2/s)	1.7×10^{-10}	1.7×10^{-10}	3.4×10^{-10}
ϵ_r	66.1	88.2	66.1
ρ (kg/m^2)	1205	2409	602
c_p (J/kg K)	2141	8564	535
k (W/m K)	0.16	1.3	0.041
c_∞ (mol/L)	1.0	8.0	0.125
L (μm)	20	10	40
T_0 (K)	298	447	596
j_s (mA/cm^2)	14	224	3.5
t_c (ms)	10	2.5	20

dimensionless numbers a^*, L^*, j_s^*, t_c^*, ν_p, Le, and C^* remained identical for Cases 1 to 3.

4.1.1. Dimensionless potential

Fig. 2(a) shows the computed electric potential $\psi(0,t)$ at the surface of electrode A as a function of time t during two consecutive galvanostatic cycles for Cases 1 to 3. As expected, the surface potential increased during charging and decreased during discharging. The temporal evolution of $\psi(0,t)$ and/or its peak value differed among the three cases considered. As previously mentioned, Case 1 featured realistic electrolyte properties and cycling conditions resulting in a maximum surface potential of 2.5 V. On the other hand, the surface potential in Case 2 reached values in excess of 3.7 V due to the different properties of a hypothetical electrolyte chosen to maintain the same dimensionless similarity parameters as in Case 1. Fig. 2(b) plots the same data shown in Fig. 2(a) in terms of dimensionless potential $\psi^*(0,t^*)$ as a function of dimensionless time t^*. It is evident that the dimensionless data for all three cases collapsed onto a single curve. Similar results were obtained at any arbitrary location in the domain (not shown).

4.1.2. Dimensionless concentration

Similarly, Fig. 3(a) shows the computed anion concentration $c_2(a/2,t)$ at the Stern/diffuse layer interface near electrode A as a function of time t for Cases 1 to 3. The computed maximum values of $c_2(a/2,t)$ for the different cases varied by nearly two orders of magnitude. This can be attributed to the differences in ion diameter a between the different cases causing large differences in c_{max}. Fig. 3(b) presents the same data in dimensionless form as $c_2^*(a^*/2,t^*)$ versus t^*. Here also, the computed dimensionless concentration $c_2^*(a^*/2,t^*)$ at the Stern/diffuse layer interface as a function of t^* collapsed onto a single curve for the three different cases considered. The maximum dimensionless concentration c_{max}^* was determined by the packing parameter ν_p as $c_{max}^* = 2/\nu_p$. Similar results were obtained at other locations in the domain as well as for the cation concentration $c_1(x,t)$ and $c_1^*(x^*,t^*)$ (not shown).

4.1.3. Dimensionless temperature

Finally, Fig. 4(a) and (b) shows the temporal evolution of the computed temperature change $T(a/2,t) - T_0$ at the Stern/diffuse layer interface and $T(L,t) - T_0$ at the centerline, respectively. Temperature oscillations about an overall temperature rise were evident at each location. Fig. 4(c) and (d) shows the same data but in dimensionless form. Here also, the dimensionless temperatures $T^*(a^*/2,t^*)$ and $T^*(L^*,t^*)$ for all three cases considered collapsed onto a single curve. Similar results were obtained at other locations in the domain (not shown). Fig. 4(c) also shows the irreversible temperature rise $T_{irr}^*(t^*)$ associated with irreversible Joule heating and given by Eq. (22) as well as the temperature oscillation amplitude $\Delta T_{rev}^*(a^*/2)$ associated with reversible heating. As expected, the slope of the overall dimensionless temperature rise was given by $j_s^{*2}/2C^*$.

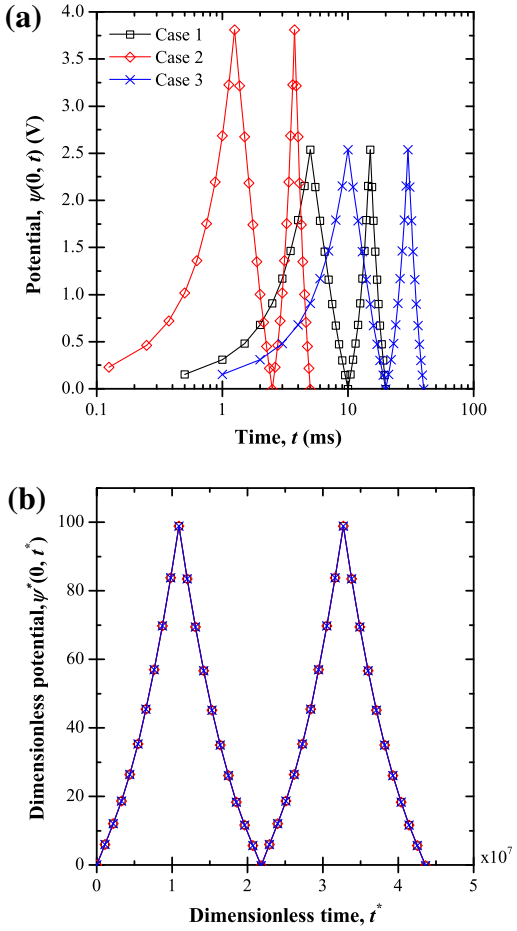

Fig. 2. Computed (a) electric potential $\psi(0,\ t)$ at the surface of electrode A as a function of time t and (b) dimensionless electric potential $\psi^*(0,t^*)$ as a function of dimensionless time t^* during two consecutive galvanostatic charging/discharging cycles for Cases 1 to 3 (Table 2).

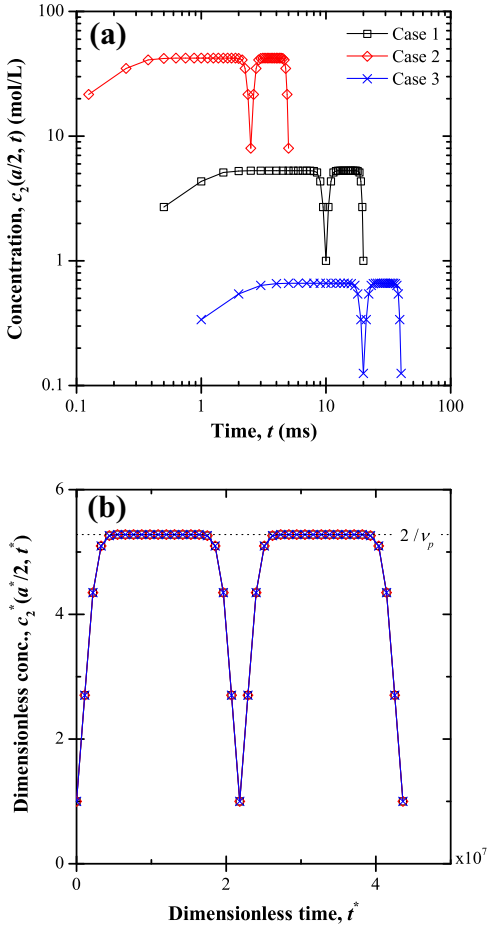

Fig. 3. Computed (a) anion concentration $c_2(a/2,t)$ at the Stern/diffuse layer interface as a function of time t and (b) dimensionless anion concentration $c_2^*(a^*/2,t^*)$ as a function of dimensionless time t^* during two consecutive galvanostatic charging/discharging cycles for Cases 1 to 3 (Table 2).

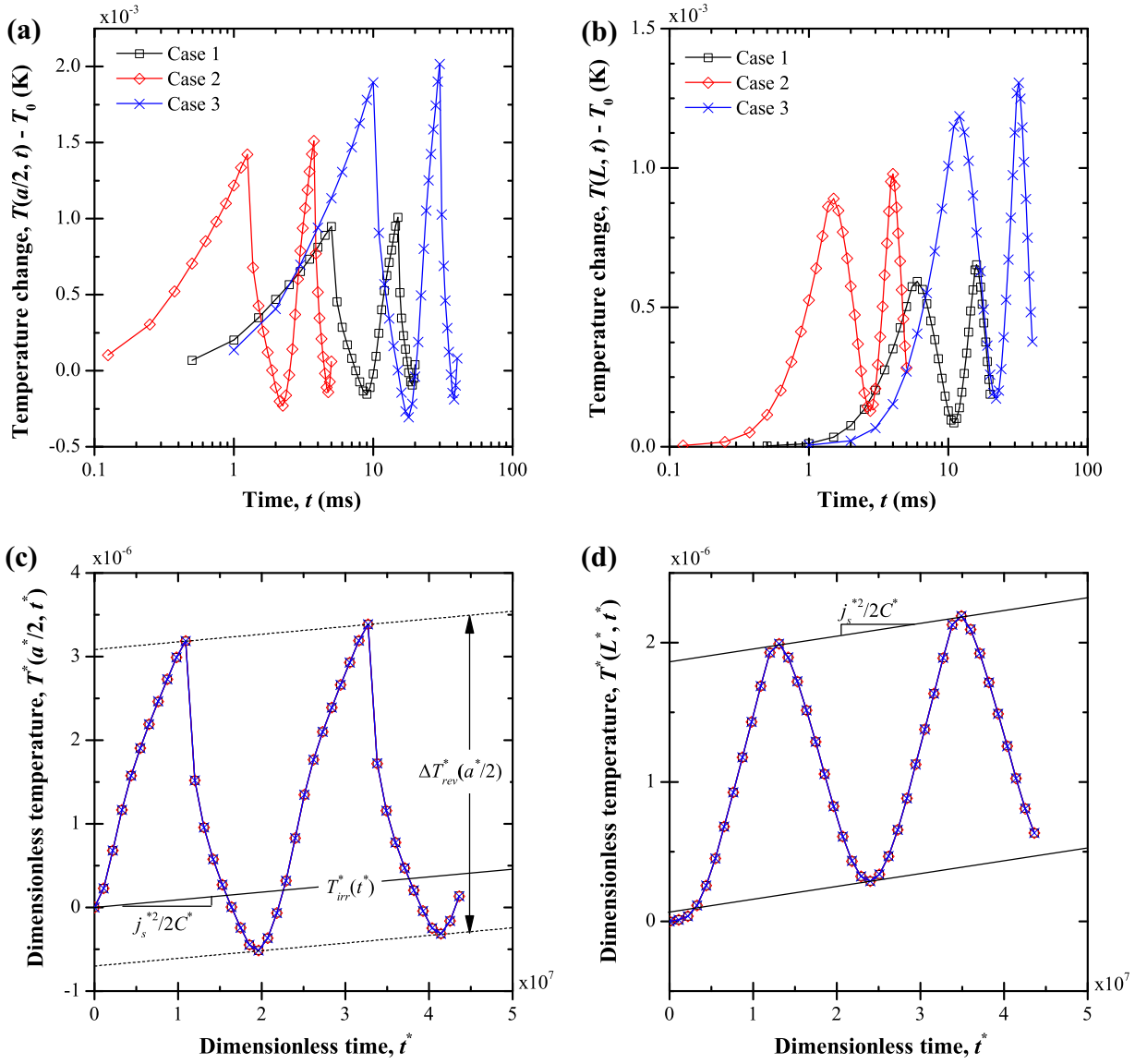

Fig. 4. Computed temperature change (a) $T(a/2,t)-T_0$ at the Stern/diffuse layer interface and (b) $T(L,t)-T_0$ at the centerline as functions of time t as well as dimensionless temperature change (c) $T^*(a^*/2,t^*)$ and (d) $T^*(L^*,t^*)$ as functions of dimensionless time t^* during two consecutive galvanostatic charging/discharging cycles for Cases 1 to 3 (Table 2).

Overall, these results illustrate the scaling analysis performed on the coupled MPNP and energy conservation equations and their initial and boundary conditions for EDLCs with binary and symmetric electrolytes under galvanostatic cycling. The dimensionless variables $\psi^*(x^*,t^*)$, $c_i^*(x^*,t^*)$, and $T^*(x^*,t^*)$ depended only on the seven similarity parameters a^*, L^*, j_s^*, t_c^*, v_p, Le, and C^*. The same observations were made for the dimensionless local volumetric heat generation rates $\dot{q}_{irr}^*$ and $\dot{q}_{rev}^*$ (see Supplementary Materials).

4.2. Scaling laws for thermal effects

4.2.1. Temperature oscillation amplitude

Table 3 summarizes three baseline sets of dimensionless similarity parameters used to develop scaling laws for ΔT_{rev}^*. Case 1 corresponds to the similarity parameters for 1 mol L^{-1} $TEABF_4$ in PC solvent, previously used to illustrate the scaling analysis. Cases 4 and 5 feature different values of a^*, L^*, j_s^*, t_c^*, v_p, Le, and C^*.

Fig. 5(a) shows $\Delta T_{rev}^*(a^*/2)$ as a function of the dimensionless heat capacity C^* varying from 78 to 735 while the other six relevant dimensionless similarity parameters are provided in Table 3. Since the reversible heat generation Q_{rev}^* does not depend on C^*, it remained identical for all points in each case. Fig. 5(a) indicates that $\Delta T_{rev}^*(a^*/2)$ was proportional to $1/C^*$. Note that this was consistent with the expression of T_{irr}^* given by Eq. (22).

Fig. 5(b) plots $\Delta T_{rev}^*(a^*/2)C^*$ as a function of the Lewis number Le ranging from 187 to 748. Here also, the similarity parameters other than Le are given in Table 3. Fig. 5(b) reveals that $\Delta T_{rev}^*(a^*/2)C^*$ was proportional to $1/Le^{1/2}$. As previously mentioned, large Lewis numbers correspond to rapid heat diffusion compared to mass diffusion. Thus, $\Delta T_{rev}^*(a^*/2)$ at the Stern/diffuse layer interface decreased as Le increased due to the increased rate of heat diffusion within the electrolyte.

Fig. 5(c) plots $\Delta T_{rev}^*(a^*/2)C^*Le^{1/2}$ as a function of Q_{rev}^* computed numerically for various values of j_s^* and v_p in the ranges $3\times10^{-7}\leqslant j_s^*\leqslant 2.4\times10^{-6}$ and $0.0012\leqslant v_p\leqslant 0.88$. It confirms that $\Delta T_{rev}^*(a^*/2)C^*Le^{1/2}$ was linearly proportional to Q_{rev}^*.

Fig. 5(d) shows $\Delta T_{rev}^*(a^*/2)C^*Le^{1/2}/Q_{rev}^*$ as a function of the cycle period t_c^* ranging from 1.2×10^6 to 4.4×10^7 with all other parameters given by Table 3. It indicates that $\Delta T_{rev}^*(a^*/2)C^*Le^{1/2}/Q_{rev}^*$ was proportional to $1/t_c^{*1/2}$ and that all cases fell on a single curve. In

Table 3
Baseline values of the seven dimensionless similarity parameters used in Fig. 5 to develop the correlation for ΔT^*_{rev} given by Eq. (25).

	Case 1	Case 4	Case 5
a^*	2.4	1.6	6.1
L^*	7.2×10^4	4.7×10^4	1.4×10^5
j_s^*	2.4×10^{-6}	8.7×10^{-6}	6.0×10^{-7}
t_c^*	2.2×10^7	9.2×10^6	4.4×10^7
ν_p	0.38	0.16	0.74
Le	374	748	281
C^*	310	735	233

fact, charging over a longer cycle period t_c^* allows more time for the heat generated to dissipate from the EDL region to the bulk electrolyte, thus reducing the maximum oscillation amplitude.

Finally, the ratio $\Delta T^*_{rev}(a^*/2)C^* Le^{1/2} t_c^{*1/2}/Q^*_{rev}$ was found to be independent of a^* and varied negligibly with L^* (see Supplementary Materials). It was approximately constant and equal to 1.3 so that the dimensionless temperature oscillation amplitude was given by

$$\Delta T^*_{rev}(a^*/2) = 1.3\frac{Q^*_{rev}}{t_c^{*1/2} Le^{1/2} C^*} = 1.3\frac{Q^*_{E,d} + Q^*_{E,s} + Q^*_{S,c}}{t_c^{*1/2} Le^{1/2} C^*}. \quad (25)$$

It can be expressed in dimensional form as

$$\Delta T_{rev}(a/2) = 1.3\frac{Q_{rev}}{(t_c k \rho c_p)^{1/2}}. \quad (26)$$

The temperature oscillation amplitude $\Delta T_{rev}(a/2)$ increased with increasing amount of reversible heat generated during the charging step Q_{rev} and with decreasing cycle period t_c, as well as decreasing electrolyte thermal effusivity defined as $e_{th} = (k\rho c_p)^{1/2}$. The latter represents the rate at which the electrolyte can absorb heat from its surroundings [39].

4.2.2. Heat generation

The scaling analysis of Section 3.3 indicated that the dimensionless volumetric heat generation rates $\dot{q}^*_{E,d}$, $\dot{q}^*_{E,s}$, and $\dot{q}^*_{S,c}$

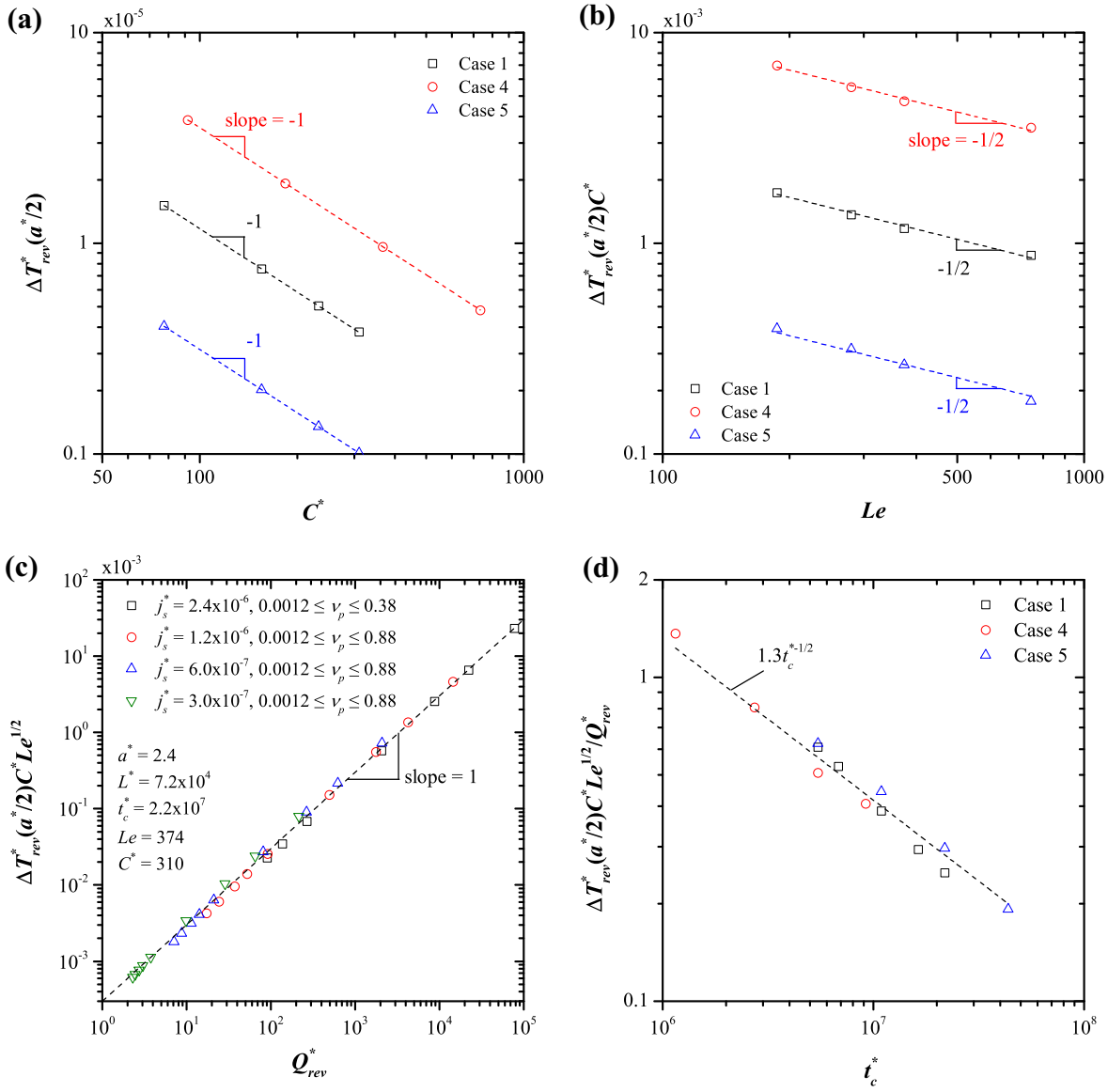

Fig. 5. Computed values of (a) $\Delta T^*_{rev}(a^*/2)$ as a function of C^*, (b) $\Delta T^*_{rev}(a^*/2)C^*$ as a function of Le, (c) $\Delta T^*_{rev}(a^*/2)C^* Le^{1/2}$ as a function of Q^*_{rev}, and (d) $\Delta T^*_{rev}(a^*/2)C^* Le^{1/2}/Q^*_{rev}$ as a function of t_c^*.

were functions of a^*, L^*, j_s^*, t_c^*, and v_p only. This section aims to derive scaling laws for $Q_{E,d}^*$, $Q_{E,s}^*$, and $Q_{S,c}^*$ as functions of these five similarity parameters to be used in Eq. (25).

First, plotting $Q_{E,d}^*$, $Q_{E,s}^*$, and $Q_{S,c}^*$ as functions of L^* and a^* indicated that the dimensionless inter-electrode spacing L^* had no effect on $Q_{E,d}^*$, $Q_{E,s}^*$, and $Q_{S,c}^*$ (see Supplementary Materials). Indeed, for sufficiently large L^*, i.e., $L^* \gg 1$, the EDLs did not overlap, and the EDL concentration profiles, responsible for reversible heating, were independent of L^* as previously observed by Wang and Pilon [19,20,40]. In addition, the heat of mixing contribution $Q_{S,c}^*$ was found to be proportional to a^{*3} while $Q_{E,d}^*$ and $Q_{E,s}^*$ were independent of a^*. This is consistent with the expressions for $\dot{q}_{E,d}^*$, $\dot{q}_{E,s}^*$, and $\dot{q}_{S,c}^*$ given by Eqs. (17) and (18). Plotting $Q_{E,d}^*$ as a function of the dimensionless product $j_s^* t_c^*$ for several combinations of v_p, j_s^*, and t_c^* showed that predictions for the same values of v_p and $j_s^* t_c^*$ overlapped despite featuring different values of j_s^* and t_c^*. This indicates that $Q_{E,d}^*$ depended only on the product $j_s^* t_c^*$ rather than on the individual parameters j_s^* and t_c^*. This was also true for $Q_{E,s}^*$ and $Q_{S,c}^*/a^{*3}$ (see Supplementary Materials).

Fig. 6(a) shows the reciprocal $1/Q_{E,d}^*$ as a function of the packing parameter v_p for various values of $j_s^* t_c^*$. It indicates that $1/Q_{E,d}^*$ was a linear function of v_p given by $1/Q_{E,d}^* = A_{E,d}(j_s^* t_c^*)v_p + B_{E,d}(j_s^* t_c^*)$ where $A_{E,d}$ and $B_{E,d}$ are semi-empirical functions of $j_s^* t_c^*$. As v_p increased and steric effects became more significant, $Q_{E,d}^*$ decreased, i.e., $1/Q_{E,d}^*$ increased. Fig. 6(b) shows the fitting functions $A_{E,d}$ and $B_{E,d}$ as functions of the product $j_s^* t_c^*$. Both could be fitted as power law functions of $j_s^* t_c^*$ so that $A_{E,d} = 0.4(j_s^* t_c^*)^{-0.6}$ and $B_{E,d} = 10(j_s^* t_c^*)^{-1.8}$. This yielded the correlation for $Q_{E,d}^*$

$$Q_{E,d}^* = \frac{1}{10(j_s^* t_c^*)^{-1.8} + 0.4(j_s^* t_c^*)^{-0.6} v_p}. \tag{27}$$

Note that in the limiting case when v_p approaches zero, $Q_{E,d}^* = 0.1(j_s^* t_c^*)^{1.8}$. This corresponds to cases when ions can be treated as point charges whose transport is governed by the Poisson–Nernst–Planck model [16].

Similarly, Fig. 7(a) plots $Q_{E,s}^*$ as a function of the packing parameter v_p for different values of $j_s^* t_c^*$. It indicates that $Q_{E,s}^*$ was (i) linearly proportional to v_p for small values of v_p and (ii) inversely proportional to v_p as v_p approached 1. The dashed lines are curve fits of the form $Q_{E,s}^* = \left[1/(A_{E,s}(j_s^* t_c^*)v_p) + v_p/B_{E,s}(j_s^* t_c^*)\right]^{-1}$ where $A_{E,s}$ and $B_{E,s}$ are functions of the product $j_s^* t_c^*$. Fig. 7(b) shows the fitting functions $A_{E,s}$ and $B_{E,s}$ versus $j_s^* t_c^*$. Both could be fitted as power laws such that $A_{E,s} = (j_s^* t_c^*)^{3.3}/680$ and $B_{E,s} = (j_s^* t_c^*)/6.7$. Then, the correlation for $Q_{E,s}^*$ can be written as

$$Q_{E,s}^* = \frac{1}{680(j_s^* t_c^*)^{-3.3} v_p^{-1} + 6.7(j_s^* t_c^*)^{-1} v_p}. \tag{28}$$

Fig. 8(a) plots $Q_{S,c}^*/a^{*3}$ as a function of v_p for various values of $j_s^* t_c^*$. It is evident that $Q_{S,c}^*/a^{*3}$ (i) was inversely proportional to v_p when v_p was small and (ii) decreased steeply towards zero as v_p approached 1. In the latter case, the behavior of $Q_{S,c}^*/a^{*3}$ can be estimated based on the expression for $\dot{q}_{S,c}^*$ given by Eq. (18) indicating that $\dot{q}_{S,c}^*$ was proportional to the concentration gradient $\partial(c_1^* + c_2^*)/\partial x^*$. This concentration gradient could be approximated in the limiting case when the dimensionless surface concentration is $c_{max}^* = 2/v_p$. Then, the dimensionless concentration sum $c_1^* + c_2^*$ decreased from $c_1^* + c_2^* = 2/v_p$ at the electrode surface to the bulk concentration $c_1^* + c_2^* = 2$ over the EDL thickness ($\Delta x^* \sim 1$) so that $\partial(c_1^* + c_2^*)/\partial x^* \sim (1 - v_p)/v_p$. Thus, Fig. 8(b) plots $Q_{S,c}^*/a^{*3}$ as a function of $(1 - v_p)/v_p$, along with dashed lines of slope 2 to guide the eye. It indicates that for small values of $(1 - v_p)/v_p$, i.e., for v_p

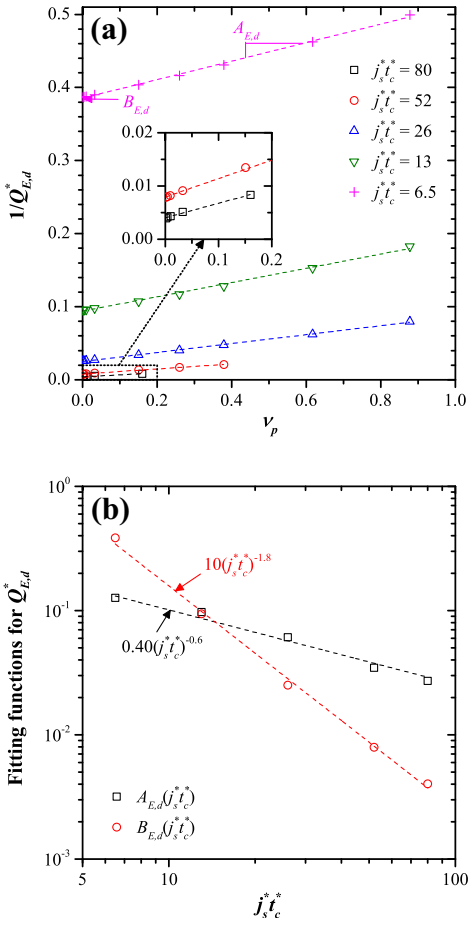

Fig. 6. (a) Computed values of $1/Q_{E,d}^*$ as a function of v_p for different values of $j_s^* t_c^*$ along with curve fits of the form $1/Q_{E,d}^* = A_{E,d}v_p + B_{E,d}$ (Eq. (27)) and (b) fitting functions $A_{E,d}$ and $B_{E,d}$ versus $j_s^* t_c^*$.

approaching unity, $Q_{S,c}^*/a^{*3}$ was proportional to $[(1 - v_p)/v_p]^2$. The data can be fitted with curve fits of the form $Q_{S,c}^*/a^{*3} = \left[v_p/A_{S,c}(j_s^* t_c^*) + v_p^2/(1 - v_p)^2 B_{S,c}(j_s^* t_c^*)\right]^{-1}$ represented by the dashed lines in Fig. 8(a). Fig. 9(a) and (b) shows the fitting functions $A_{S,c}$ and $B_{S,c}$, respectively, as functions of $j_s^* t_c^*$. They were fitted as $A_{S,c} = (j_s^* t_c^*)^{2.7}/6700$ and $B_{S,c} = 0.0095 j_s^* t_c^* - 0.045$. Thus, the correlation for $Q_{S,c}^*$ can be expressed as

$$Q_{S,c}^* = \frac{a^{*3}}{6700 v_p (j_s^* t_c^*)^{-2.7} + 100(0.95 j_s^* t_c^* - 4.5)^{-1}[(1 - v_p)/v_p]^{-2}}. \tag{29}$$

The above scaling laws for $\Delta T_{rev}^*(a^*/2)$ and for $Q_{E,d}^*$, $Q_{E,s}^*$, and $Q_{S,c}^*$ were derived for a wide range of dimensionless parameters, namely, $1.2 \leqslant a^* \leqslant 29$, $3.6 \times 10^4 \leqslant L^* \leqslant 2.2 \times 10^5$, $3.0 \times 10^{-7} \leqslant j_s^* \leqslant 8.7 \times 10^{-6}$, $1.2 \times 10^6 \leqslant t_c^* \leqslant 8.7 \times 10^7$, $0.0012 \leqslant v_p \leqslant 0.88$, $187 \leqslant Le \leqslant 748$, and $78 \leqslant C^* \leqslant 735$. Note that $Q_{E,d}^*$, $Q_{E,s}^*$, and $Q_{S,c}^*$ given by Eqs. (27)–(29) could predict those computed numerically with average relative error of 5%, 20%, and 46%, respectively, as well as ΔT_{rev}^* given by Eq. (25) with average relative error of 12% (see Supplementary Materials).

The correlations for the reversible heating terms $Q_{E,d}^*$, $Q_{E,s}^*$, and $Q_{S,c}^*$ given by Eqs. (27)–(29) offer several interesting insights into the reversible heating in an EDLC. In particular, $Q_{E,d}^*$, $Q_{E,s}^*$, and $Q_{S,c}^*/a^{*3}$ were all found to be functions of $j_s^* t_c^* = j_s t_c/zFc_\infty \lambda_D = j_s t_c/(\epsilon_0 \epsilon_r R_u T_0 c_\infty/2)^{1/2}$ and $v_p = 2N_a a^3 c_\infty$ only. This indicates that

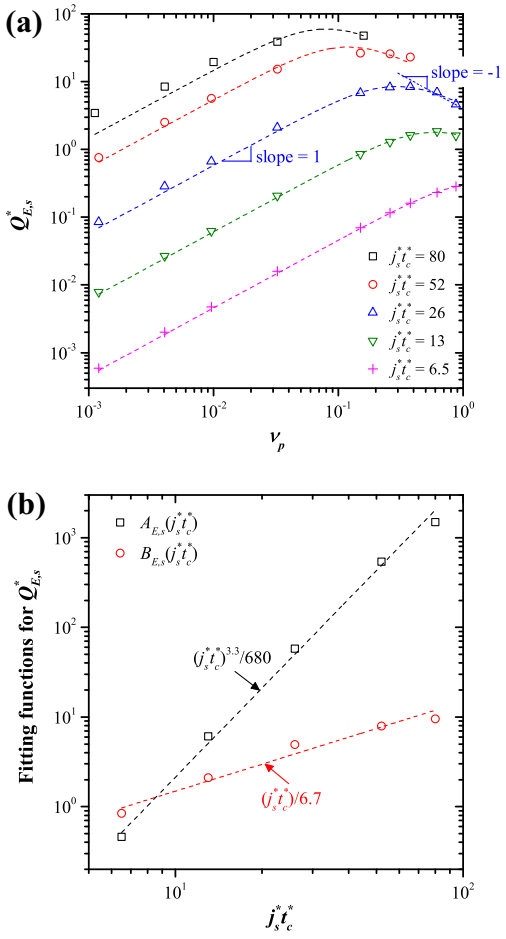

Fig. 7. (a) Computed values of $Q_{E,s}^*$ as a function of ν_p for different values of $j_s^* t_c^*$ along with curve fits of the form $Q_{E,s}^* = \left[1/A_{E,s}\nu_p + \nu_p/B_{E,s}\right]^{-1}$ (Eq. (28)) and (b) fitting functions $A_{E,s}$ and $B_{E,s}$ versus $j_s^* t_c^*$.

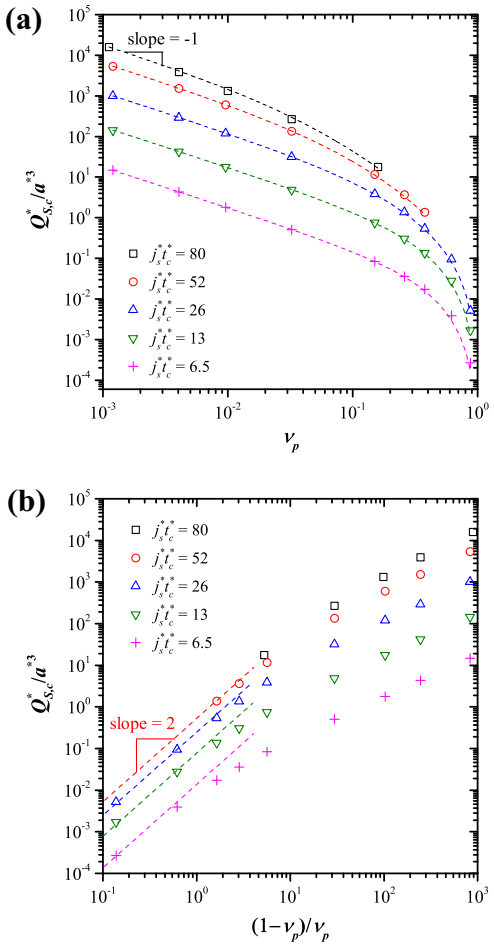

Fig. 8. Computed $Q_{S,c}^*/a^{*3}$ as a function of (a) ν_p, along with curve fits of the form $Q_{S,c}^*/a^{*3} = \left[\nu_p/A_{S,c} + \nu_p^2/(1-\nu_p)^2 B_{S,c}\right]^{-1}$ (Eq. (29)), and (b) $(1-\nu_p)/\nu_p$ for different values of $j_s^* t_c^*$.

the amount of reversible heat generated during a charging step Q_{rev} depended only on the electrolyte properties and on the amount of charge added to the EDLC corresponding to $\Delta q_s = j_s t_c/2$ (in C/m^2). In addition, the amount of reversible heat consumed during the discharging step is equal to $-Q_{rev}$. This implies that the net reversible heating in an EDLC is zero over a complete charge–discharge cycle. This is true even if the charging current density and discharging current density differ, since the total charge would remain the same. In addition, $Q_{E,d}$ and $Q_{E,s}$ (in dimensional form) were proportional to z^{-1} while $Q_{S,c}$ was proportional to z^2. This is consistent with the expressions for $\dot{q}_{E,d}$ and $\dot{q}_{E,s}$ (Eq. (8)), depending on z^{-1} through the electrical conductivity σ. By contrast, the dependence of $Q_{S,c}$ on the valency z was weaker than that of the local volumetric heat generation rate $\dot{q}_{S,c}$ (Eq. (9)) which is proportional to z^3. This difference can be attributed to the fact that the ion fluxes $\mathbf{N}_1$ and $\mathbf{N}_2$ are approximately proportional to z^{-1}. As a result, the heat of mixing contributed the most to the reversible heat generation rate for electrolytes featuring large valency z. Interestingly, the diffusion coefficient D did not affect the amount of reversible heat generated per charging step represented by Q_{rev}. This was due to the fact that, although D appears in the numerator of the expressions for $\dot{q}_{E,d}$ and $\dot{q}_{E,s}$ (Eq. (8)), the electrical conductivity σ, appearing in the denominator, is also proportional to D.

4.2.3. Thermal behavior of porous electrodes

The above scaling laws were derived from simulations of planar electrodes while, in practice, EDLC electrodes are porous. Previous studies using equilibrium models found that electrodes with radii of curvature larger than 40 nm yielded the same areal capacitance as planar electrodes [34,40]. This suggests that applying scaling laws for planar electrodes to electrodes with large enough pores is a reasonable approximation. However, the choice of surface area used to define the surface current density j_s must be carefully considered. Indeed, in contrast to planar electrodes, the surface areas of the separator and of the porous electrode differ significantly [6]. Based on charge conservation, the average current density at the electrode surface should equal $j_s = I_s/A_{el}$, where I_s is the current (in A) imposed at the current collector and A_{el} is the accessible surface area of the porous electrode (in m^2).

EDLC electrodes often feature mesopores and micropores smaller than 40 nm [3]. For such systems, the above scaling laws for planar electrodes could be corrected by a factor accounting for the morphology of the electrode. In fact, Wang et al. [41] successfully modeled the integral capacitance of nanoporous carbon electrodes as the product of the theoretical planar-electrode capacitance and a function depending only on the average pore radius in the electrode and on the effective ion diameter scaled by the Debye length. In addition, the dielectric constant ϵ_r

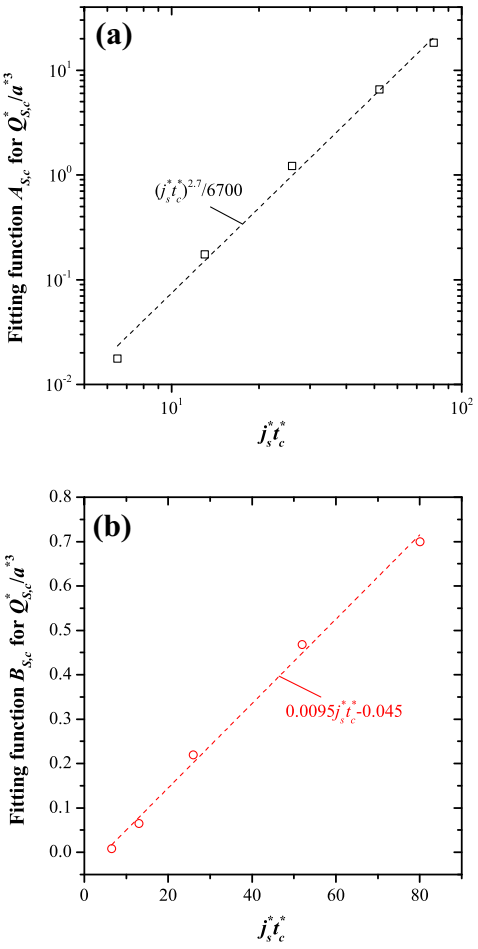

Fig. 9. Fitting functions (a) $A_{S,c}$ and (b) $B_{S,c}$ versus $j^*_s t^*_c$ in the expression for $Q^*_{S,c}/a^{*3}$ given by Eq. (29).

decreases under large electric fields typical of those found near electrode/electrolyte interfaces in EDLCs [42]. However, here, ϵ_r was assumed to be constant to facilitate the scaling analysis. Wang et al. [41] also made this assumption and showed that the effect of field-dependent relative permittivity was indirectly accounted for by the semi-empirical constants appearing in the correlation. A similar approach could be used to extend the present model to predict the heat generation rates and temperature oscillations in actual porous electrodes. To do so, a broad range of experimental data for various porous electrode structures and electrolytes would be required to validate this approach. However, this falls beyond the scope of the present study. Moreover, experimental temperature data currently available in the literature for EDLCs would be insufficient to rigorously identify a correction factor for porous electrodes and demonstrate the validity of any scaling analysis [4–6,10,23–25]. Indeed, most of the data were collected on commercial EDLC devices [4–6,10,25] whose electrolyte composition and electrode morphologies are not readily available.

5. Conclusion

In this paper, scaling analysis was performed on a recent thermal model derived from first principles for EDLCs with binary and symmetric electrolyte under galvanostatic cycling [13]. The scaling analysis reduced the design problem from twelve independent dimensional parameters to seven physically meaningful dimensionless similarity parameters governing coupled electrodiffusion and thermal transport in EDLC electrolyte. Scaling laws characterizing the maximum temperature fluctuations and the total irreversible and reversible heat generated during a charging step were developed for planar electrodes. These expressions can predict the heat generation and temperature behavior for various realistic electrolytes and cycling conditions without having to perform sophisticated and time-consuming numerical simulations. These dimensionless numbers and the scaling laws provide a framework that can be used for developing design rules and thermal management strategies for actual EDLCs.

6. Conflict of interest

None declared.

Acknowledgments

This material is based upon work supported by the National Science Foundation Graduate Research Fellowship under Grant No. DGE-1144087 and as part of the Molecularly Engineered Energy Materials, an Energy Frontier Research Center funded by the U.S. Department of Energy, Office of Science, Office of Basic Energy Sciences under Award Number DE-SC0001342.

Appendix A. Supplementary data

Supplementary data associated with this article can be found, in the online version, at http://dx.doi.org/10.1016/j.ijheatmasstransfer.2014.04.001.

References

[1] B. Conway, Electrochemical Supercapacitors: Scientific Fundamentals and Technological Applications, Kluwer Academic/Plenum Publishers, New York, NY, 1999.
[2] US Department of Energy, Basic Research Needs for Electrical Energy Storage: Report of the Basic Energy Sciences Workshop for Electrical Energy Storage, Tech. rep., Office of Basic Energy Sciences, DOE, 2007. <http://www.osti.gov/accomplishments/documents/fullText/ACC0330.pdf>.
[3] T. Pandolfo, V. Ruiz, S. Sivakkumar, J. Nerkar, Supercapacitors: Materials, Systems, and Applications, Wiley-VCH Verlag, Weinheim, Germany, 2013 (Chapter 2).
[4] J.R. Miller, Electrochemical capacitor thermal management issues at high-rate cycling, Electrochim. Acta 52 (4) (2006) 1703–1708.
[5] H. Gualous, H. Louahlia-Gualous, R. Gallay, A. Miraoui, Supercapacitor thermal modeling and characterization in transient state for industrial applications, IEEE Trans. Ind. Appl. 45 (3) (2009) 1035–1044.
[6] J. Schiffer, D. Linzen, D.U. Sauer, Heat generation in double layer capacitors, J. Power Sources 160 (1) (2006) 765–772.
[7] P. Guillemet, Y. Scudeller, T. Brousse, Multi-level reduced-order thermal modeling of electrochemical capacitors, J. Power Sources 157 (1) (2006) 630–640.
[8] P. Liu, M. Verbrugge, S. Soukiazian, Influence of temperature and electrolyte on the performance of activated-carbon supercapacitors, J. Power Sources 156 (2006) 712–718.
[9] F. Rafik, H. Gualous, R. Gallay, A. Crausaz, A. Berthon, Frequency, thermal and voltage supercapacitor characterization and modeling, J. Power Sources 165 (2) (2007) 928–934.
[10] M. Al Sakka, H. Gualous, J. Van Mierlo, H. Culcu, Thermal modeling and heat management of supercapacitor modules for vehicle applications, J. Power Sources 194 (2) (2009) 581–587.
[11] O. Bohlen, J. Kowal, D.U. Sauer, Ageing behaviour of electrochemical double layer capacitors: Part II. Lifetime simulation model for dynamic applications, J. Power Sources 173 (1) (2007) 626–632.
[12] R. Kötz, P. Ruch, D. Cericola, Aging and failure mode of electrochemical double layer capacitors during accelerated constant load tests, J. Power Sources 195 (3) (2010) 923–928.
[13] A.L. d'Entremont, L. Pilon, First-principles thermal modeling of electric double layer capacitors under constant-current cycling, J. Power Sources 246 (2014) 887–898.
[14] A. Bard, L. Faulkner, Electrochemical Methods: Fundamentals and Applications, John Wiley & Sons, New York, NY, 2001.
[15] V. Bagotsky, Fundamentals of Electrochemistry, John Wiley & Sons, Hoboken, NJ, 2006.
[16] M.S. Kilic, M.Z. Bazant, A. Ajdari, Steric effects in the dynamics of electrolytes at large applied voltages: II. Modified Poisson–Nernst–Planck equations, Phys. Rev. E 75 (2) (2007) 021503.
[17] J.S. Newman, K.E. Thomas-Alyea, Electrochemical Systems, third ed., John Wiley & Sons, Hoboken, NJ, 2004.

[18] T. Engel, P. Reid, Thermodynamics, Statistical Thermodynamics, and Kinetics, second ed., Prentice Hall, Upper Saddle River, NJ, 2010.
[19] H. Wang, L. Pilon, Intrinsic limitations of impedance measurements in determining electric double layer capacitances, Electrochem. Acta 63 (2012) 55–63.
[20] H. Wang, L. Pilon, Physical interpretation of cyclic voltammetry for measuring electric double layer capacitances, Electrochim. Acta 64 (2012) 130–139.
[21] F.P. Incropera, D.P. DeWitt, T.L. Bergman, A.S. Lavine, Fundamentals of Heat and Mass Transfer, sixth ed., John Wiley & Sons, Hoboken, NJ, 2007.
[22] B.J. Kirby, Micro- and Nanoscale Fluid Mechanics: Transport in Microfluidic Devices, Cambridge University Press, New York, NY, 2010.
[23] C. Pascot, Y. Dandeville, Y. Scudeller, P. Guillemet, T. Brousse, Calorimetric measurement of the heat generated by a double-layer capacitor cell under cycling, Thermochim. Acta 510 (2010) 53–60.
[24] Y. Dandeville, P. Guillemet, Y. Scudeller, O. Crosnier, L. Athouel, T. Brousse, Measuring time-dependent heat profiles of aqueous electrochemical capacitors under cycling, Thermochim. Acta 526 (2011) 1–8.
[25] H. Gualous, H. Louahlia, R. Gallay, Supercapacitor characterization and thermal modelling with reversible and irreversible heat effect, IEEE Trans. Power Electron. 26 (11) (2011) 3402–3409.
[26] A.G. Pandolfo, A.F. Hollenkamp, Carbon properties and their role in supercapacitors, J. Power Sources 157 (2006) 11–27.
[27] K. Radeke, K. Backhaus, A. Swiatkowski, Electrical conductivity of activated carbons, Carbon 29 (1991) 122–123.
[28] A. Subrenat, J. Baléo, P. Le Cloirec, P. Blanc, Electrical behaviour of activated carbon cloth heated by the Joule effect: desorption application, Carbon 39 (2001) 707–716.
[29] M.S. Kilic, M.Z. Bazant, A. Ajdari, Steric effects in the dynamics of electrolytes at large applied voltages: I. Double-layer charging, Phys. Rev. E 75 (2007) 021502.
[30] J.H. Masliyah, S. Bhattacharjee, Electrokinetic and Colloid Transport Phenomena, John Wiley & Sons, Hoboken, NJ, 2006.
[31] H. Wang, A. Thiele, L. Pilon, Simulations of cyclic voltammetry for electric double layers in asymmetric electrolytes: a generalized modified Poisson–Nernst–Planck model, J. Phys. Chem. C 117 (2013) 18286–18297.
[32] COMSOL, Inc., COMSOL Multiphysics Reference Guide, COMSOL 4.2 ed., 2011.
[33] J. Chmiola, G. Yushin, Y. Gogotsi, C. Portet, P. Simon, P. Taberna, Anomalous increase in carbon capacitance at pore sizes less than 1 nanometer, Science 313 (5794) (2006) 1760–1763.
[34] H. Wang, L. Pilon, Mesoscale modeling of electric double layer capacitors with three-dimensional ordered structures, J. Power Sources 221 (2013) 252–260.
[35] W.M. Haynes (ed), CRC Handbook of Chemistry and Physics, 92nd ed., CRC Press, Boca Raton, FL, 2011.
[36] M. Tuliszka, F. Jaroszyk, M. Portalski, Absolute measurement of the thermal conductivity of propylene carbonate by the AC transient hot-wire technique, Int. J. Thermophys. 12 (5) (1991) 791–800.
[37] E.Y. Tyunina, V.N. Afanasiev, M.D. Chekunova, Electroconductivity of tetraethylammonium tetrafluoroborate in propylene carbonate at various temperatures, J. Chem. Eng. Data 56 (7) (2011) 3222–3226.
[38] A. Burke, Ultracapacitors: why, how, and where is the technology, J. Power Sources 91 (2000) 37–50.
[39] A. Salazar, On thermal diffusivity, Eur. J. Phys. 24 (2003) 351–358.
[40] H. Wang, L. Pilon, Accurate simulations of electric double layer capacitance of ultramicroelectrodes, J. Phys. Chem. C 115 (2011) 16711–16719.
[41] H. Wang, J. Fang, L. Pilon, Scaling laws for carbon-based electric double layer capacitors, Electrochim. Acta 109 (2013) 316–321.
[42] F. Booth, Dielectric constant of polar liquids at high field strengths, J. Chem. Phys. 23 (3) (1955) 453–457.